Plasma Chem Plasma Process (2008) 28:85–105
DOI 10.1007/s11090-007-9109-8

ORIGINAL PAPER

Effects of the Length of a Cylindrical Solid Shield on the Entrainment of Ambient Air into Turbulent and Laminar Impinging Argon Plasma Jets

Hai-Xing Wang · Xi Chen · Wenxia Pan

Received: 6 July 2007 / Accepted: 24 October 2007 / Published online: 8 November 2007

Abstract When materials processing is conducted in air surroundings by use of an impinging plasma jet, the ambient air will be entrained into the materials processing region, resulting in unfavorable oxidation of the feedstock metal particles injected into the plasma jet and of metallic substrate material. Using a cylindrical solid shield may avoid the air entrainment if the shield length is suitably selected and this approach has the merit that expensive vacuum chamber and its pumping system are not needed. Modeling study is thus conducted to reveal how the length of the cylindrical solid shield affects the ambient air entrainment when materials processing (spraying, remelting, hardening, etc.) is conducted by use of a turbulent or laminar argon plasma jet impinging normally upon a flat substrate in atmospheric air. It is shown that the mass flow rate of the ambient air entrained into the impinging plasma jet cannot be appreciably reduced unless the cylindrical shield is long enough. In order to completely avoid the air entrainment, the gap between the downstream-end section of the cylindrical solid shield and the substrate surface must be carefully selected, and the suitable size of the gap for the turbulent plasma jet is appreciably larger than that for the laminar one. The overheating of the solid shield or the substrate could become a problem for the turbulent case, and thus additional cooling measure may be needed when the entrainment of ambient air into the turbulent impinging plasma jet is to be completely avoided.

Keywords Impinging plasma jet · Air entrainment · Solid-shield effect · Materials processing · Modeling

H.-X. Wang
School of Astronautics, Beijing University of Aeronautics and Astronautics, Beijing 100083, China

X. Chen (✉)
Department of Engineering Mechanics, Tsinghua University, Beijing 100084, China
e-mail: cx-dem@mail.tsinghua.edu.cn

W. X. Pan
Institute of Mechanics, Chinese Academy of Sciences, Beijing 100080, China

Introduction

When materials processing (plasma spraying, remelting, hardening, etc.) is conducted in atmospheric air surroundings by use of a turbulent or laminar plasma jet impinging normally upon a substrate (or workpiece), the ambient air will be entrained into the materials processing region, leading to the oxidation of the metallic particles injected into the plasma jet and of the metallic substrate material, while the material oxidation is often not desirable for many cases. According to our previous study [1], for the typical case that the maximum temperature and velocity at the inlet center of an argon plasma jet are 14,000 K and 1,000 m/s, the distance between the plasma jet inlet and the substrate is 80 mm whereas the radius of substrate is 50 mm, a large amount of ambient air would be entrained into the impinging argon plasma jets if no solid or gas shield was employed to prevent the air entrainment: The maximum mass flow rate of the ambient air entrained into the laminar impinging plasma jet was shown to be 2.6 times as large as the argon mass flow rate at the jet inlet, while its turbulent counterpart was even much larger, i.e. the maximum mass flow rate of the ambient air entrained into the turbulent impinging plasma jet was 18 times as large as the argon mass flow rate at the jet inlet. Wang et al. [1] also revealed such an important fact that the existence of the substrate significantly enhanced the maximum mass flow rate of the entrained ambient air due to the additional contribution to the air entrainment of the wall jet formed along the substrate surface. For the typical case mentioned above, the substrate causes the enhancement of maximum entrained-air mass flowrate 5.47 times larger for the laminar impinging plasma jet, while 1.56 times larger for the turbulent impinging plasma jet in comparison with corresponding free jets (without accounting for the existence of the substrate) [1]. Such a predicted result is quite different from that of [2], in which it was claimed that the existence of the substrate would reduce (instead of increase) the mass flow rate of surrounding gas entrained into the turbulent plasma jet.

In order to reduce the unfavorable effect of the ambient air entrainment, using a chamber enclosing the whole material processing region was suggested and studied numerically [3], but it can only be applied to a fixed small-size substrates and thus is not applicable to the case where materials processing is continuously conducted by laterally moving the substrate with respect to the incident plasma jet. Using a shrouding gas and/or solid shield to screen the plasma jet was proposed and adopted in plasma spraying, showing appreciable improvement of coating quality [4–8]. In order to better understand the effectiveness of adding shrouding gas, modeling studies were conducted in [2, 9, 10]. It is anticipated that although the shrouding gas can affect appreciably the flow of the ambient air entrained into the upstream region of the main plasma jet and thus the oxidation of metallic particles injected into the plasma jet can be lessened to a certain extent, it is not too useful to avoid the oxidation of metallic substrate since the shrouding gas cannot prevent effectively the air entrainment into the wall jet region developed along the substrate surface. Another approach to screen the plasma jet is using a conical hollow metallic or ceramic shield [2], which is placed co-axially with the plasma jet and actually represents a conical extension of the anode-nozzle of the plasma torch, as shown schematically in Fig. 1. A drawback of employing such a conical solid shield is that its inner wall surface contacts directly with the hot plasma jet and thus an effective cooling measure must be adopted to prevent the solid shield from overheating. Using a cylindrical solid shield as shown schematically in Fig. 2 may avoid such an overheating problem at least when the axial length of solid shield is comparatively short, and thus the present study is concerned with the case with a cylindrical solid shield. It is expected that if the length of the

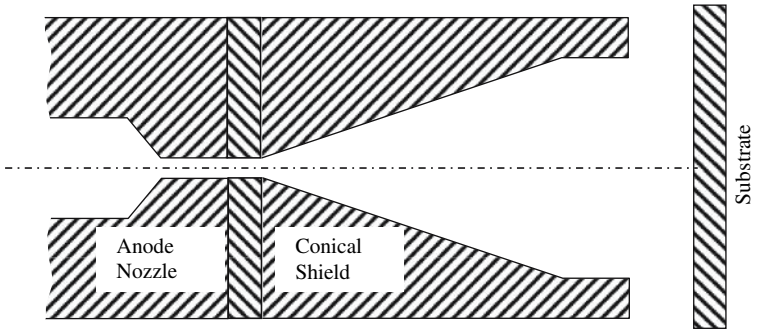

Fig. 1 Schematic diagraph of the conical shield as studied in [2]

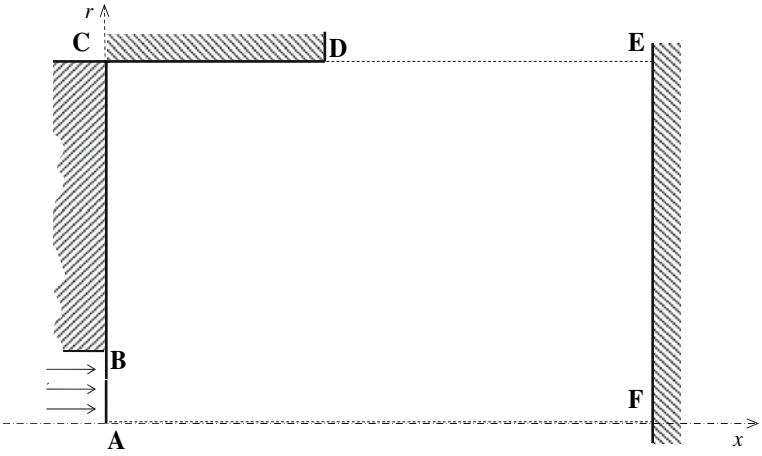

Fig. 2 Schematic diagraph of the jet system and the computational domain. A–B is the jet inlet or plasma torch exit, B–C the rear wall of torch, C–D the cylindrical solid shield, D–E the free boundary, E–F the substrate, whereas A–F is the jet axis

cylindrical shield or the size of the gap between the downstream-end section of the cylindrical solid shield and the substrate surface (D–E in Fig. 2) is selected suitably, only the working gas can outflow from the cylindrical solid shield while the ambient air cannot enter the material processing region. The present paper aims at studying how the length of the cylindrical solid shield affects the entrainment of ambient air into the impinging plasma jet and determining the shield size suitable to avoid completely the material oxidation for both the turbulent and laminar impinging argon plasma jets by using a modeling approach.

Modeling Approach

Almost the same modeling approach as used in [1] is employed in the present study. The main change is concerned with the employment of the boundary conditions at the lateral boundary of the impinging plasma jet. Since a cylindrical solid shield is used here and partially covers the lateral boundary, the solid-wall boundary conditions will be used at

the solid shield surface (C–D in Fig. 2), whereas the free boundary conditions are still used for other part of the lateral boundary not being covered by the shield (D–E in Fig. 2), in order to reveal the effects of the cylindrical solid shield on the impinging plasma jet characteristics, especially on the entrainment of ambient air into the impinging argon plasma jets.

The main assumptions employed in this study include (i) argon is used as the working gas to generate the plasma jet; (ii) the flow is subsonic, steady and axi-symmetrical; (iii) the plasma is in the local thermodynamic equilibrium (LTE) state and optically thin to radiation; (iv) the swirling velocity component is negligible; and (v) the diffusion of the surrounding air into the argon plasma jet, if any, can be handled using the turbulence-enhanced combined-diffusion-coefficient method [11] for the turbulent case and using the combined-diffusion-coefficient method [12, 13] for the laminar case.

Based on the foregoing assumptions, the conservation equations for mass, momentum, energy, species, turbulent kinetic energy and its dissipation rate can be written for the *turbulent* plasma jet case as follows [1, 11, 14]:

$$\frac{\partial}{\partial x}(\rho u)+\frac{1}{r}\frac{\partial}{\partial r}(r\rho v)=0 \tag{1}$$

$$\frac{\partial(\rho uu)}{\partial x}+\frac{1}{r}\frac{\partial(r\rho uv)}{\partial r}=-\frac{\partial p}{\partial x}+2\frac{\partial}{\partial x}\left[(\mu+\mu_T)\frac{\partial u}{\partial x}\right]+\frac{1}{r}\frac{\partial}{\partial r}\left[r(\mu+\mu_T)\left(\frac{\partial u}{\partial r}+\frac{\partial v}{\partial x}\right)\right] \tag{2}$$

$$\begin{aligned}\frac{\partial(\rho uv)}{\partial x}+\frac{1}{r}\frac{\partial(r\rho vv)}{\partial r}=&-\frac{\partial p}{\partial r}+\frac{2}{r}\frac{\partial}{\partial r}\left[r(\mu+\mu_T)\frac{\partial v}{\partial r}\right]+\frac{\partial}{\partial x}\left[(\mu+\mu_T)\left(\frac{\partial v}{\partial x}+\frac{\partial u}{\partial r}\right)\right]\\&-2(\mu+\mu_T)\frac{v}{r^2}\end{aligned} \tag{3}$$

$$\begin{aligned}\frac{\partial(\rho uh)}{\partial x}+\frac{1}{r}\frac{\partial(r\rho vh)}{\partial r}=&\frac{\partial}{\partial x}\left[\left(\frac{k}{C_p}+\frac{\mu_T}{\sigma_h}\right)\frac{\partial h}{\partial x}\right]+\frac{1}{r}\frac{\partial}{\partial r}\left[r\left(\frac{k}{C_p}+\frac{\mu_T}{\sigma_h}\right)\frac{\partial h}{\partial r}\right]-U_r\\&-\frac{\partial}{\partial x}[(h_A-h_B)J_x]-\frac{1}{r}\frac{\partial}{\partial r}[r(h_A-h_B)J_r]\\&-\frac{\partial}{\partial x}\left[\frac{k}{c_P}(h_A-h_B)\frac{\partial f_A}{\partial x}\right]-\frac{1}{r}\frac{\partial}{\partial r}\left[r\frac{k}{c_P}(h_A-h_B)\frac{\partial f_A}{\partial r}\right]\\&+u\frac{\partial p}{\partial x}+v\frac{\partial p}{\partial r}\\&+(\mu+\mu_T)\left\{2\left[\left(\frac{\partial u}{\partial x}\right)^2+\left(\frac{\partial v}{\partial r}\right)^2+\left(\frac{v}{r}\right)^2\right]+\left(\frac{\partial u}{\partial r}+\frac{\partial v}{\partial x}\right)^2\right\}\end{aligned} \tag{4}$$

$$\frac{\partial(\rho uf_A)}{\partial x}+\frac{1}{r}\frac{\partial(r\rho vf_A)}{\partial r}=\frac{\partial}{\partial x}\left[\left(\frac{\mu_T}{\sigma_f}+\Gamma_f\right)\frac{\partial f_A}{\partial x}\right]+\frac{1}{r}\frac{\partial}{\partial r}\left[r\left(\frac{\mu_T}{\sigma_f}+\Gamma_f\right)\frac{\partial f_A}{\partial r}\right]+S_f \tag{5}$$

$$\frac{\partial(\rho uK)}{\partial x}+\frac{1}{r}\frac{\partial(rv\rho K)}{\partial r}=\frac{\partial}{\partial x}\left[\left(\mu+\frac{\mu_T}{\sigma_K}\right)\frac{\partial K}{\partial x}\right]+\frac{1}{r}\frac{\partial}{\partial r}\left[r\left(\mu+\frac{\mu_T}{\sigma_K}\right)\frac{\partial K}{\partial r}\right]+G-\rho\varepsilon \tag{6}$$

$$\frac{\partial(\rho u\varepsilon)}{\partial x}+\frac{1}{r}\frac{\partial(rv\rho\varepsilon)}{\partial r}=\frac{\partial}{\partial x}\left[\left(\mu+\frac{\mu_T}{\sigma_\varepsilon}\right)\frac{\partial\varepsilon}{\partial x}\right]+\frac{1}{r}\frac{\partial}{\partial r}\left[r\left(\mu+\frac{\mu_T}{\sigma_\varepsilon}\right)\frac{\partial\varepsilon}{\partial r}\right]+\frac{\varepsilon}{K}(C_1G-C_2\rho\varepsilon) \tag{7}$$

All the physical quantities appearing in those equations are their time-averaged values; u and v are the axial (x-) and radial (r-) velocity components; p the pressure; f_A the mass fraction of argon in the argon–air mixture; K and ε are the turbulent kinetic energy and its dissipation rate; ρ, h, μ, k, c_p and U_r are the temperature- and composition-dependent

plasma density, specific enthalpy, molecular viscosity, thermal conductivity, specific heat at constant pressure and radiation power per unit volume of plasma, respectively. In Eq. 4, the last three terms represent the pressure work and viscous dissipation, which can be neglected only at low Mach numbers (e.g. for Ma < 0.3); all the terms containing $(h_A - h_B)$ represent the contribution of species diffusion to the energy transport [11, 14], where h_A and h_B are the temperature-dependent specific enthalpies of gases A (argon) and B (air), respectively; J_x and J_r are the axial and radial components of the following argon (species A) diffusion mass flux vector [1, 11–15]

$$\mathbf{J}_A = -\frac{\mu_T}{\sigma_f}\nabla f_A - \left(n^2/\rho\right)\overline{m}_A\overline{m}_B\overline{D}^x_{AB}\nabla X_A - \overline{D}^T_{AB}\nabla \ln T \tag{8}$$

in which the first term on the right-hand side is the turbulent diffusion term [11], n is the total gas-particle number density, $\overline{m}_A$ and $\overline{m}_B$ are the averaged gas-particle masses for all the heavy particles (excluding electrons) coming from argon (i.e. species A) and those from air (i.e. species B), X_A is the molar fraction of argon in the argon–air mixture, whereas $\overline{D}^x_{AB}$ and $\overline{D}^T_{AB}$ are the combined ordinary diffusion coefficient associated with the argon mole-fraction gradient, ∇X_A, and the combined thermal diffusion coefficient associated with the temperature gradient, ∇T, respectively [12, 13]. The molecular transport coefficient Γ_f in the species conservation equation (5) can be expressed as $\Gamma_f = [\overline{m}_A\overline{m}_B/(\overline{M}\overline{M}_A)]\rho\overline{D}^x_{AB}$, in which $\overline{M}$ and $\overline{M}_A$ are the averaged gas-particle mass for all the gas particles (including electrons) of the gas mixture and that for all the gas particles coming from argon, respectively [12]. The source term S_f in Eq. 5 can be expressed as [1, 11, 14, 15]

$$\begin{aligned} S_f = &\frac{1}{r}\frac{\partial}{\partial r}\left(r\Gamma_f\frac{f_A}{\overline{M}}\frac{\partial\overline{M}}{\partial r}\right) - \frac{1}{r}\frac{\partial}{\partial r}\left(r\Gamma_f\frac{f_A}{\overline{M}_A}\frac{\partial\overline{M}_A}{\partial r}\right) + \frac{\partial}{\partial x}\left(\Gamma_f\frac{f_A}{\overline{M}}\frac{\partial\overline{M}}{\partial x}\right) \\ &- \frac{\partial}{\partial x}\left(\Gamma_f\frac{f_A}{\overline{M}_A}\frac{\partial\overline{M}_A}{\partial x}\right) + \frac{1}{r}\frac{\partial}{\partial r}\left(r\overline{D}^T_{AB}\frac{\partial\ln T}{\partial r}\right) + \frac{\partial}{\partial x}\left(\overline{D}^T_{AB}\frac{\partial\ln T}{\partial x}\right) \end{aligned} \tag{9}$$

The turbulence generation term, G, in Eqs. 6 and 7 is calculated by

$$G = \mu_T\left[2\left(\frac{\partial u}{\partial x}\right)^2 + 2\left(\frac{\partial v}{\partial r}\right)^2 + 2\left(\frac{v}{r}\right)^2 + \left(\frac{\partial u}{\partial r} + \frac{\partial v}{\partial x}\right)^2\right] \tag{10}$$

μ_T is the turbulent viscosity and is calculated by $\mu_T = C_\mu\rho K^2/\varepsilon$ when the K-ε two-equation turbulence model is employed. C_μ, C_1, C_2, σ_h, σ_f, σ_K and σ_ε are constants in the turbulence model, and in this study they are taken to be their commonly adopted values, i.e. 0.09, 1.44, 1.92, 0.9, 1.0, 1.0 and 1.3, respectively.

On the other hand, for the study of the characteristics of *laminar* argon plasma jets impinging normally upon a flat substrate located in ambient air, Eqs. 1–5 are still be employed but all the turbulent transport terms are deleted by setting $\mu_T = 0$. Namely, $(\mu_T + \mu)$ in Eqs. 2 and 3 is substituted by μ, $[(\mu_T/\sigma_h) + (k/c_p)]$ in Eq. 4 is substituted by k/c_p, and $[(\mu_T/\sigma_f) + \Gamma_f]$ in Eq. 5 is substituted by Γ_f. Equations 6 and 7 are not used for the laminar case.

The computational domain used in the modeling is denoted as A-B-C-D-E-F-A in Fig. 2. A–B is the plasma jet inlet and the jet-inlet radius is taken to be 4 mm. C–D represents the cylindrical solid shield used to reduce ambient air entrainment, and its axial size (L_S) can be changed in this study to reveal the effects of solid-shield size on the air entrainment. D–E is the lateral free boundary of the impinging plasma jet. E–F is the flat

substrate impinged by the plasma jet, and the radial size (EF or AC) of the computational domain is taken at first to be 50 mm, corresponding to typical conditions of plasma materials processing. The axial size (CE or AF) will be called the substrate standoff distance and denoted by L hereafter.

The boundary conditions used in the present study are as follows:

(i) At the jet inlet (A–B in Fig. 2): $v = 0$, $f_A = 1.0$, and the following radial profiles of axial velocity and plasma temperature are used:

$$u = U_0[1 - (r/R)^{1.4}], \quad T = (T_0 - T_w)[1 - (r/R)^{2.3}] + T_w \tag{11}$$

in which R is the radius of the jet inlet (4 mm), T_w is the inner wall temperature of plasma torch and taken to be T_w = 1,000 K, whereas U_0 and T_0 are the maximum axial velocity and temperature at jet-inlet center (U_0 will be called the jet-inlet velocity and T_0 the jet-inlet temperature hereafter), respectively. For the turbulent cases, $K = 0.00005 \times u_{in}^2$ and $\varepsilon = K^{3/2}/L_T$ are used at the jet inlet section A–B, where $L_T = 0.075\delta_{0.1}/C_\mu^{3/4}$ and $\delta_{0.1}$ is the jet width defined by the radial distance at which the axial velocity reduces to $u = 0.1 \times U_0$ [11, 16]. The jet-inlet axial-velocity and temperature profiles (11) were employed in a few previous studies [11, 16] and were shown to be able to predict plasma temperature, velocity and species concentration fields in reasonable agreement with corresponding experimental data [16, 17] for a typical turbulent argon plasma jet (U_0 = 1,092 m/s and T_0 = 12,913 K) issuing into the ambient air. For facilitating the comparison of turbulent and laminar plasma jet characteristics, the same jet-inlet velocity and temperature profiles are used in this study for both the laminar and turbulent plasma jets, as in [1, 14].

(ii) At the rear wall surface B–C of the plasma torch, for the laminar case, $u = v = 0$ and zero diffusion flux are employed, and the wall temperature is assumed to vary in the radial direction according to the relation $T = 1000 - 500 \cdot [\ln(r/R)/\ln(R_{out}/R)]$, in which R and R_{out} are the inner-radius and outer-radius of the plasma torch wall. For the turbulent jet case, wall function method is used to treat the B–C boundary conditions.

(iii) Along the lateral boundary C–E, the following conditions are employed: For the case with $x \le L_S$ (L_S is the axial length of the cylindrical solid shield), i.e. at the inner surface of the cylindrical solid shield (C–D), $u = v = 0$, zero diffusion flux and the constant wall temperature condition

$$T = T_{w,sh} = 500 \text{ K} \tag{12a}$$

are used for the laminar case, and the wall function method is adopted for the turbulent case. On the other hand, for the case with $x > L_S$, i.e. at the lateral free boundary D–E, the following boundary conditions are employed:

$$\partial u/\partial r = 0, \quad \partial(\rho r v)/\partial r = 0$$

and

$$\text{if } v < 0: \ T = 300\,\text{K}, \ f_A = 0, \ K = 0, \ \varepsilon = 0 \tag{12b}$$

$$\text{if } v > 0: \partial h/\partial r = 0, \ \partial f_A/\partial r = 0, \ \partial K/\partial r = 0, \ \partial \varepsilon/\partial r = 0$$

(iv) At the substrate surface E–F, for the laminar impinging plasma jet case, $u = v = 0$ and zero diffusion flux are employed and the wall temperature is assumed to be 500 K. For the turbulent jet case, the wall function method is also used.

(v) Along the jet axis A–F, the following axisymmetrical conditions are employed:

$$\partial\phi/\partial r = 0 \ (\phi = u, h, f_A, K, \varepsilon), \quad v = 0 \tag{13}$$

The SIMPLER algorithm [18] is used to solve the governing equations (1)–(7) associated with correspondent boundary conditions to obtain the velocities, specific enthalpy, argon mass fraction and turbulent parameter (for turbulent case) fields in the impinging plasma jets. In the SIMPLER algorithm, the control volume and finite difference methods are employed; the combined convection–diffusion terms are discretised using the power-law scheme formulated based on the exact solution of the one-dimensional convection–diffusion equation; the source terms are discretised using the central difference scheme; and under-relaxation factors are employed in the iterative solution processes [18]. After the convergent results of the specific enthalpy and argon mass fraction distributions have been obtained, the temperature field in the plasma jets can be easily calculated using the argon-air plasma property tables compiled for different temperatures (300–30,000 K with interval 100 K) and for different argon mass fractions at atmospheric pressure [13]. The grid points employed in the computation are 180 (x-) × 78 (r-direction). Non-uniform mesh is adopted with finer mesh spacing near the plate surface, the jet inlet and the jet axis. A special numerical test shows that mesh-independent results have been obtained using the 180 × 78 mesh.

Results and Discussion

Typical computed results are presented in Figs. 3–13 concerning the effects of the extension length of cylindrical solid shield (L_S) on the characteristics of the turbulent and laminar argon plasma jets impinging normally upon the flat substrate in atmospheric air for the case with substrate standoff distance L = 100 mm, the jet-inlet velocity U_0 = 1000 m/s and the jet-inlet temperature T_0 = 14,000 K. For this typical case, the Mach number at the jet-inlet center is 0.456, whereas the argon mass flow rate and the plasma jet power are 1.087×10^{-3} kg/s and 8.12 kW (the estimated torch input power is thus about 16–24 kW), respectively.

Figure 3(a–c) compares the computed isolines of plasma temperature, axial velocity and argon mass-fraction, respectively, in the turbulent impinging plasma jets without the solid shield (lower semi-planes) and with a cylindrical solid shield of extension length L_S = 40 mm (upper semi-planes). Corresponding comparisons are shown in Fig. 4(a–c) for their laminar counterparts. Figures 3 and 4 show that the axial decaying-rates of plasma temperature, axial velocity and argon mass fraction in the turbulent impinging plasma jets (Fig. 3) are much larger than their laminar counterparts (Fig. 4), because the turbulent transport mechanism dominant in the turbulent jets is much more effective than the molecular transport mechanism in the laminar jet [1, 14]. It is also seen from Figs. 3 and 4 that the isoline distributions in the upper semi-planes are almost the same as those in the lower semi-planes for both the turbulent and laminar impinging plasma jets. This fact implies that when the extension length of cylindrical solid shield is comparatively short (e.g. for the case with shield length L_S = 40 mm shown in the upper semi-planes of Figs. 3 and 4), the plasma parameter distributions (isotherms, isovels and f_A isolines) within the turbulent or laminar impinging plasma jets are almost not influenced by the existence of the cylindrical solid shield or the cylindrical shield with length L_S = 40 mm cannot reduce the entrainment of ambient air into the plasma jets.

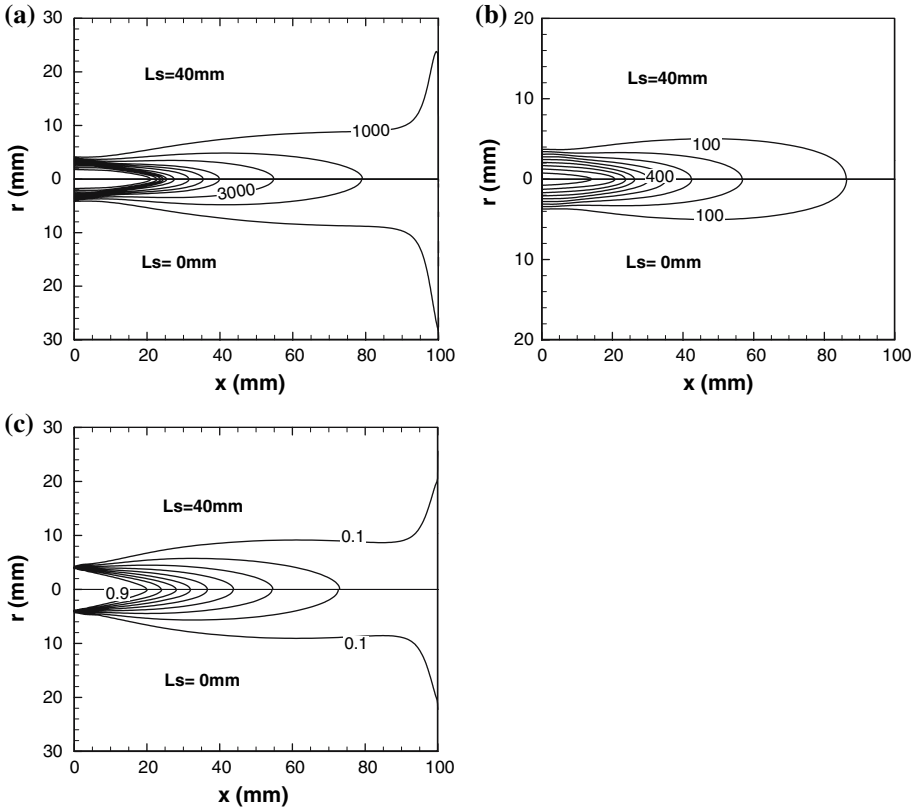

Fig. 3 Comparison of the computed isolines of temperature (**a**), axial velocity (**b**) and argon mass fraction (**c**) in the turbulent impinging plasma jet for the case with a cylindrical solid shield of 40 mm length (upper semi-planes) to those without shield (lower semi-planes)

It is expected that with the increase of the extension length L_S of the cylindrical solid shield, the effect of the solid shield on the characteristics of the impinging plasma jets may become somewhat more appreciable. The computed results presented in Figs. 5–8 indeed demonstrate this expectation. Figure 5(a–d) shows the variation with the shield length L_S of the computed streamlines in the turbulent impinging plasma jets. The extension lengths of the cylindrical solid shield are taken to be $L_S = 0$, 20, 40, 60, 80, 90 and 95 mm, respectively. It is seen clearly from Fig. 5 that with the increase of the shield length L_S, marked change appears in the flow pattern within the region covered by the cylindrical solid shield: When the solid shield is employed ($L_S \geq 20$ mm), a toroidal recirculation vortex appears near the corner between the shield wall and the torch rear-wall, whereas the axial size of the recirculation vortex appearing in the flow field lengthens with the increase of the shield length. It is noted that near the downstream end of the cylindrical solid shield, the cold ambient air entrained into the region inside the cylindrical solid shield at first flows towards the frontal part of the plasma jet (with axial velocity $u < 0$) and then changes its flow direction to $u > 0$ and co-flows with the main jet towards the substrate. An exciting result is that the total mass flow rate of the ambient air entrained into the turbulent

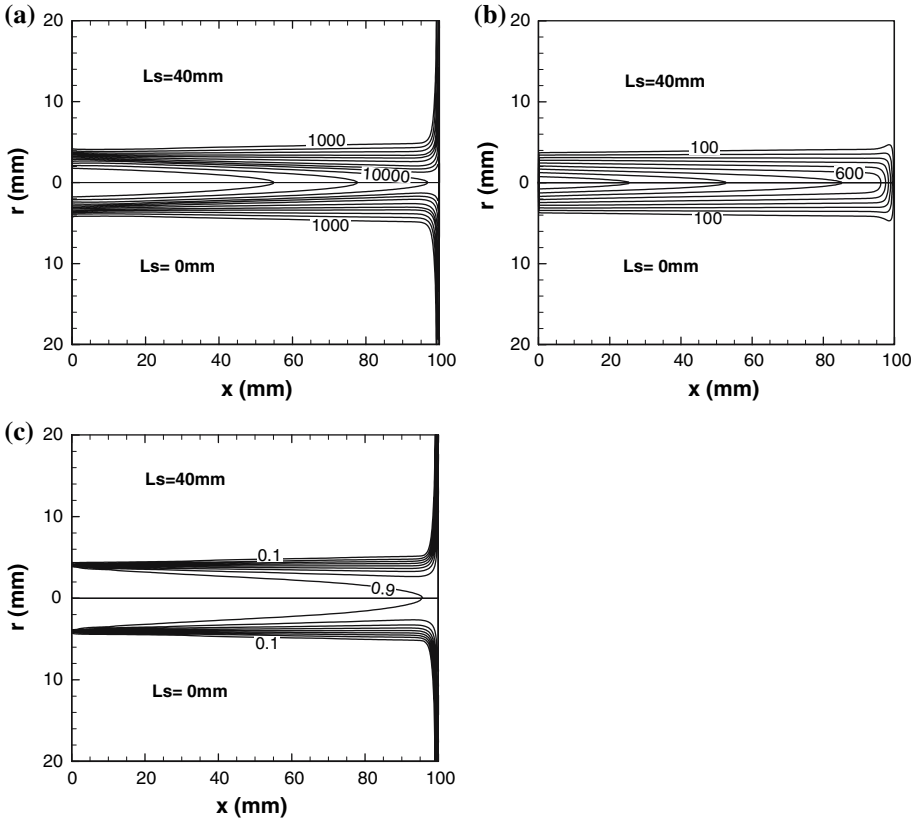

Fig. 4 Comparison of the computed isolines of temperature (**a**), axial velocity (**b**) and argon mass fraction (**c**) in the laminar impinging plasma jet for the case with a cylindrical solid shield of 40 mm length (upper semi-planes) to those without shield (lower semi-planes)

impinging plasma jet is less influenced by the shield length L_S in the range of L_S = 0–70 mm (the substrate standoff distance is fixed to be L = 100 mm), as demonstrated by counting the numbers of the streamlines with mass flow-rate interval 4×10^{-4} kg/s per radian. After the shield length L_S is $\geq$80 mm, the mass flow rate of the ambient air entrained into the turbulent impinging plasma jet decreases with increasing shield length, and the flow pattern changes to the form with only one large recirculation vortex when L_S is $\geq$90 mm. For the case with L_S = 95 mm, no ambient air can enter into the turbulent impinging plasma jet and all the working gas coming from the plasma jet inlet outflows radially from gap between the downstream-end section of cylindrical solid shield and the substrate surface, and the computed streamlines and isotherms for this case are shown in the upper and lower semi-planes of Fig. 5(d). Figure 6(a–c) compares the variations of the computed plasma temperature, axial velocity and argon mass fraction along the axis of the turbulent impinging plasma jet for different shield lengths. It is shown that when $L_S <$ 95 mm, the plasma temperature, axial velocity and argon mass fraction at the jet axis decrease monotonically with increasing axial distance from the jet inlet. The axial profiles of the plasma temperature, axial velocity and argon mass fraction are less influenced by the shield lengths if the shield lengths are less than about 80 mm since corresponding mass

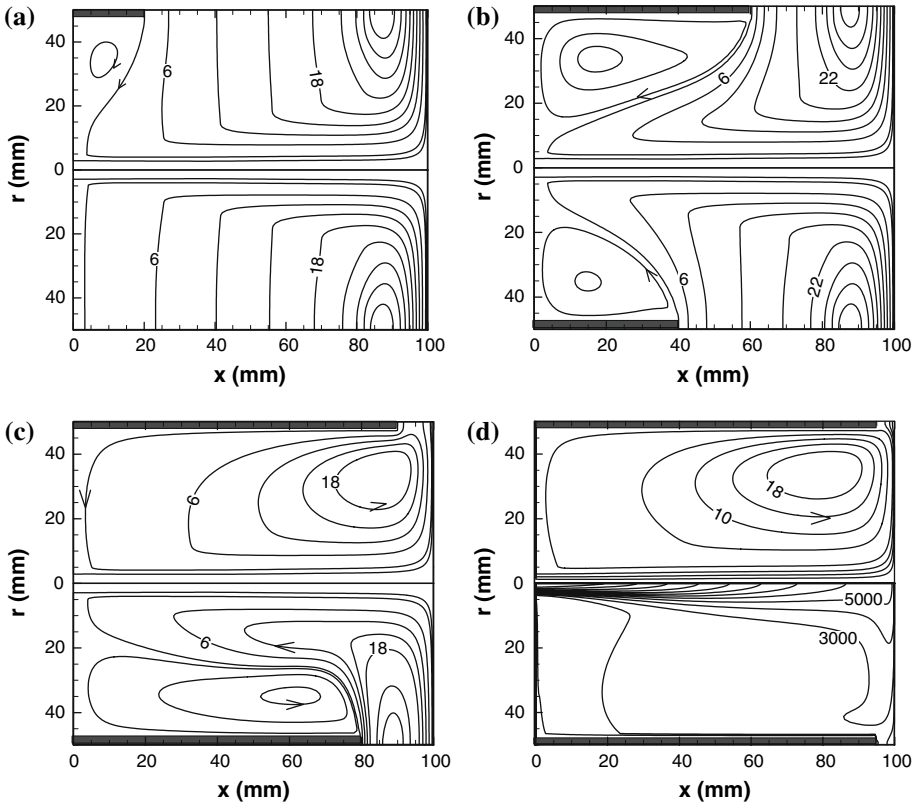

Fig. 5 Comparison of the computed streamlines in the turbulent impinging plasma jet for the cases with shield lengths L_S = 0 mm (lower semi-plane in *a*), 20 mm (upper semi-plane in *a*), 40 mm (lower semi-plane in *b*), 60 mm (upper semi-plane in *b*), 80 mm (lower semi-plane in *c*), 90 mm (upper semi-plane in *c*) and 95 mm (upper semi-plane in *d*). Lower semi-plane in *d* is the computed isotherms for L_S = 95 mm. Stream line interval is 4×10^{-4} kg/s per radian

flow rates of entrained ambient air are less influenced by the shield length, as shown in Fig. 5(a–c). When the shield length increases to 90 mm, Fig. 6(a–c) shows that the axial decaying-rates of the plasma temperature, axial velocity and argon mass fraction somewhat decreases due to that less ambient air is entrained into the turbulent impinging plasma jet, as seen in Fig. 5(c). On the other hand, when the extension length of the cylindrical solid shield increases to 95 mm (noting that the substrate standoff distance is L = 100 mm and thus the width of the gap between the downstream-end section of cylindrical solid shield and the substrate surface is 5 mm), Fig. 6(c) shows that the argon mass fractions are 1.0 everywhere, demonstrating that no ambient air is entrained into the turbulent impinging plasma jet. Even for this case with L_S = 95 mm (or L_S/L = 0.95), the plasma temperature at the jet axis still decreases with increasing axial distance due to the existence of heat transfer between the plasma flow and the colder constricted walls (including the substrate and the solid shield), but with appreciably reduced axial decaying-rate due to nonexistence of the cold air entrainment. Those results are consistent with our guess deduced from the computed streamlines shown in Fig. 5(a–d). Although creating a gap of 5 mm between the downstream-end section of cylindrical solid shield and the substrate surface is not difficult in practice and thus employing a cylindrical solid shield with the gap ($L - L_S$) = 5 mm to

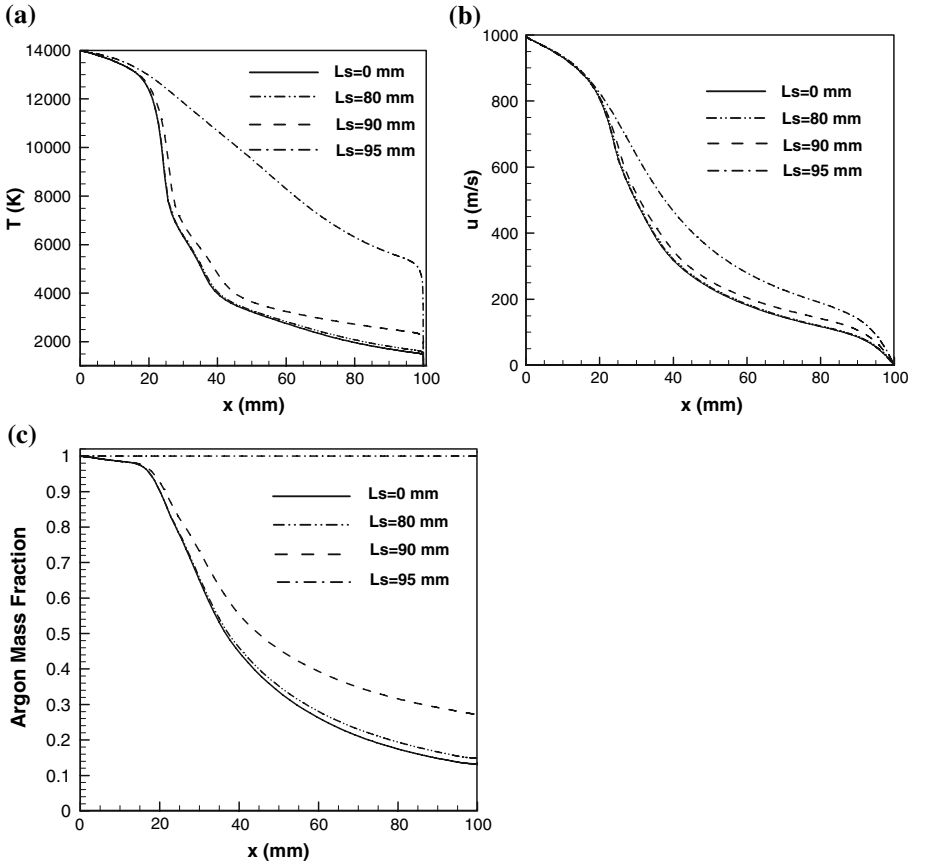

Fig. 6 Comparison of the computed variation of plasma temperature (**a**), axial velocity (**b**) and argon mass fraction (**c**) along the axis of the turbulent impinging plasma jet for the cases with shield lengths of 0, 80, 90 and 95 mm

avoid completely the air entrainment and substrate oxidation is feasible in the turbulent plasma materials processing, one has to consider the overheating problem of the solid shield as shown later on. It is because that when the gap ($L - L_S$) decreases to 5 mm, the solid shield will be heated directly by the recirculating high temperature argon due to the dramatic change of the flow pattern (as seen in Fig. 5(d)); while the solid shield can be effectively protected from overheating by the entrained cold ambient air if the gap ($L - L_S$) is $\geq$10 mm. Another problem maybe also encountered is the overheating of the substrate, since the plasma temperature at the outer edge of the thermal boundary layer on the substrate is comparatively high and thus the heat flux to the substrate is also comparatively large for the case with L_S = 95 mm as seen in Fig. 6(a). It is well known that for fixed substrate thickness and standoff distance as well as fixed jet inlet conditions, the magnitude and distribution of the substrate temperature are controlled by the substrate moving speed and the external cooling condition at the back face of the substrate. Hence, substrate moving speed and external cooling should be somewhat enhanced to maintain a desirable lower substrate temperature at the higher plasma-substrate heat flux for L_S = 95 mm.

Corresponding modeling results are presented in Figs. 7 and 8 about the effects of different solid shield lengths on the characteristics of the laminar impinging plasma jets for the case U_0 = 1,000 m/s, T_0 = 14,000 K and L = 100 mm. Figure 7(a–d) shows the variation with the shield length L_S of the computed streamlines in the laminar impinging plasma jets. The shield lengths are taken to be L_S = 0, 20, 40, 60, 80, 90 and 99 mm, respectively, for the present laminar case. It is seen that totally the flow patterns for the laminar impinging jet are similar to those shown in Fig. 5 for the turbulent case, and the difference is only due to much less entrainment rate being involved in the laminar impinging plasma jet [1, 14]. It is noted that the total mass flow rate of the ambient air entrained into the laminar impinging plasma jet is less influenced by the shield length L_S in the range of L_S = 0–90 mm. However, when the shield length increases to 99 mm (or L_S/L = 0.99), a quite different flow pattern appears, i.e. ambient air cannot enter into the laminar impinging plasma jet and all the working gas coming from the plasma jet inlet outflows radially from the gap between the downstream-end section of cylindrical solid shield and the substrate surface, and the computed streamlines and isotherms for this case are shown in the upper and lower semi-planes of Fig. 7(d). For L_S = 99 mm, there also

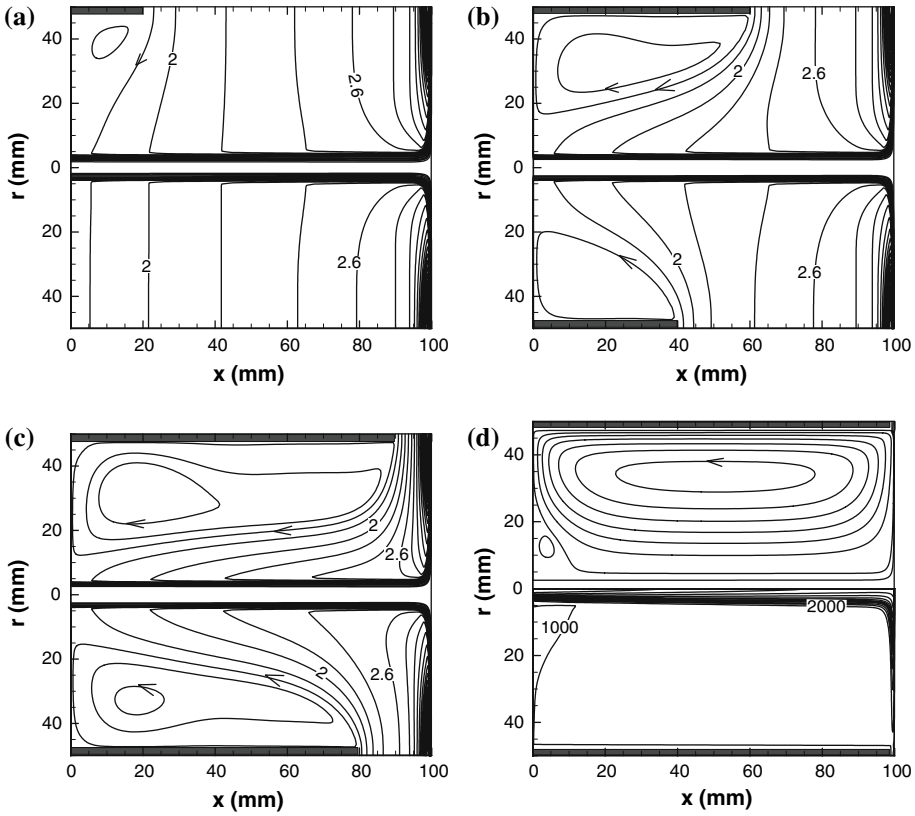

Fig. 7 Comparison of the computed streamlines in the laminar impinging plasma jet for the cases with shield length L_S = 0 mm (lower semi-plane in *a*), 20 mm (upper semi-plane in *a*), 40 mm (lower semi-plane in *b*), 60 mm (upper semi-plane in *b*), 80 mm (lower semi-plane in *c*), 90 mm (upper semi-plane in *c*) and 99 mm (upper semi-plane in *d*). Lower semi-plane in *d* is the computed isotherms for L_S = 99 mm. Stream line interval is 2×10^{-5} kg/s per radian

exists a very large closed gas recirculation vortex in the flow field. Figure 8(a–c) compares the computed variation of the plasma temperature, axial velocity and argon mass fraction along the axis of the laminar impinging plasma jet for different extension lengths of the cylindrical solid shield. It is shown that the plasma temperature, axial velocity and argon mass fraction at the jet axis also decrease monotonically with increasing axial distance from the jet inlet, but with appreciably smaller decaying-rates than their turbulent counterparts shown in Fig. 6(a–c) due to that molecular transport in the laminar plasma jet is much less efficient than the turbulent transport dominant in the turbulent plasma jet. The axial profiles are less influenced by the shield lengths for the laminar impinging plasma jet if the lengths are less than about 90 mm. When the extension length L_S of the cylindrical solid shield increases to 99 mm (for substrate standoff distance L = 100 mm), Fig. 8(c) shows that the argon mass fractions are 1.0 everywhere, demonstrating that indeed no ambient air is entrained into the laminar impinging plasma jet for this case. Even for such a case (L_S = 99 mm) without air entrainment, the plasma temperature at the jet axis still decreases with increasing axial distance also due to the existence of heat transfer between the plasma flow and the colder constricted walls, but the axial decaying-rate of plasma temperature is appreciably less than the case with $L_S \leq 90$ mm due to nonexistence of air entrainment for the case with L_S = 99 mm. These results are also consistent with our guess

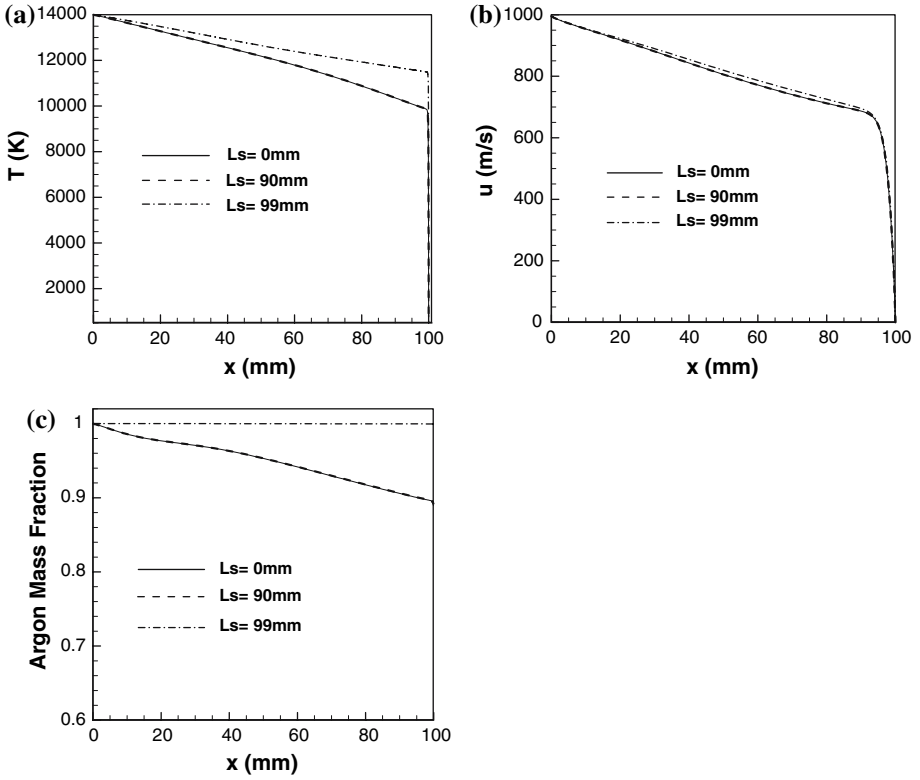

Fig. 8 Comparison of the computed variation of plasma temperature (**a**), axial velocity (**b**) and argon mass fraction (**c**) along the axis of the laminar impinging plasma jet for the cases with shield lengths L_S = 0, 90 and 99 mm

deduced from the computed streamlines shown in Fig. 7(a–d). Since keeping a constant gap between the downstream-end section of cylindrical solid shield and the substrate surface as small as 1 mm is not convenient technologically when the substrate is continuously moving laterally, it is better to use a somewhat larger gap but employ an additional measure, e.g. adding a shrouding gas axially injected from the rear end of the cylindrical solid shield, to avoid the air entrainment and substrate oxidation in the laminar plasma materials processing.

From their intuitive judgment, researchers often consider that employing a cylindrical solid shield can always reduce the mass flow rate of ambient air entrained into the impinging plasma jets. However, the computed results presented in Figs. 5–8 for the turbulent and laminar impinging plasma jets demonstrate that the cylindrical solid shield cannot reduce appreciably the ambient air entrainment if the solid shield length is not long enough. For example, for the case with substrate standoff distance $L = 100$ mm, the cylindrical solid shield cannot appreciably reduce the ambient air entrainment if the shield length $L_S < \sim 70$ mm for the turbulent impinging plasma jet or if $L_S < \sim 90$ mm for the laminar impinging plasma jet. In order to reveal this fact more clearly, Fig. 9(a) compares the axial variations of the net increase of axial mass flux in the turbulent impinging plasma jets calculated by

$$F_e = F - F_0 = 2\pi \int_0^{R_{out}} \rho u r \, dr - \left(2\pi \int_0^{R} \rho u r \, dr \right)_{inlet} \tag{14}$$

for different shield lengths. Here $(2\pi \int_0^R \rho u r \, dr)_{inlet}$ is the argon mass flow rate at the jet inlet and thus F_e expresses the net increase of the axial mass flux of the impinging jet at the section with axial distance x after subtracting the mass flow rate at the jet inlet (F_0) from the total axial mass flux (F) at the same x section. Figure 9(a) shows that for the case without the solid shield, initially the net increase of axial mass flux, F_e, in the turbulent impinging plasma jet increases monotonously with increasing axial distance but rapidly decreases in the near-substrate region since the substrate forces the jet change its flow direction from axial to radial direction. F_e even takes a negative value at the substrate surface, representing that all the gas including that coming from the jet inlet radially leaves the computational domain. The maximum value of the net increase of axial mass flux F_e appears at the section about 12 mm ahead from the substrate surface. It is interesting to note that the axial distance at which the net increase of axial mass flux (F_e) begin to assume rising values is just corresponding to the shield lengths when $L_S \leq$ 80 mm. For example, for the shield length equaling to 40 mm, corresponding axial distance at which F_e begins to rise is also 40 mm. However, such a computed result does not mean that no ambient air is entrained into the upstream region (with axial distance less than 40 mm) of the turbulent plasma main-jet when the shield length $L_S = 40$ mm. In fact, the mass flow rates of the ambient air entrained into the main jet region with shield length $L_S = 40$ mm is almost equal to that for the case without the solid shield (i.e. $L_S = 0$ mm), as mentioned above. The reason is that a part of cold ambient air entrained into the impinging jet for $L_S = 40$ mm at first flows toward the frontal part of the plasma jet (axial velocity $u < 0$) and then changes its flow direction to $u > 0$ and co-flows with the main jet toward the substrate, resulting in that the net increase of axial mass flux calculated by Eq. 14 assumes zero value until the axial distance increases to 40 mm. Only when the shield length increases to 95 mm, no cold ambient air can be entrained into the plasma jet, and thus the substrate oxidation can be avoided. In order to reveal the effects of the shield length on the air entrainment into the main jet region,

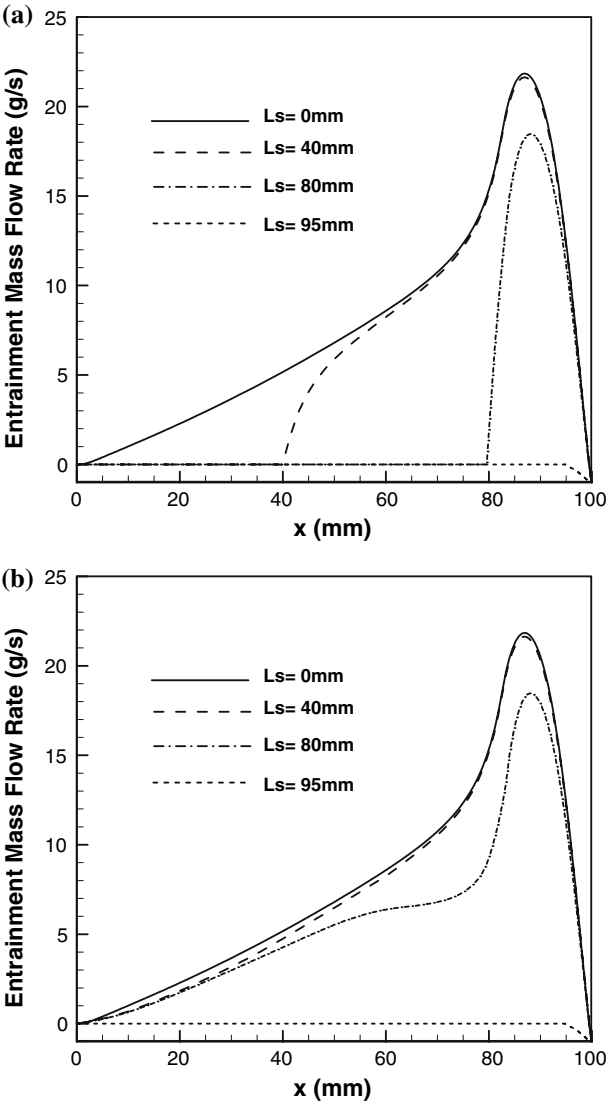

Fig. 9 Comparison of the computed variation with the axial distance of the net increase of axial mass fluxes in the turbulent impinging plasma jet (**a**) and in the main jet region (**b**) for the cases with shield lengths L_S = 0, 40, 80 and 95 mm

Fig. 9(b) shows the axial variation of the net increase in the axial mass flux of main jet ($F_{e,main\ jet}$) calculated by

$$F_{e,main\,jet} = F_{main\,jet} - F_0 = \left(2\pi \int_0^{R_{u=0}} \rho u r\, dr\right)_{u>0} - \left(2\pi \int_0^{R} \rho u r\, dr\right)_{inlet} \tag{15}$$

Namely, the net increase in the axial mass flux of main jet ($F_{e,main\ jet}$) is obtained after the axial mass flux at the jet inlet (F_0) is subtracted from the total axial mass flux of the main jet ($F_{main\ jet}$). Here the total axial mass flux of the main jet, $F_{main\,jet}$ =

$(2\pi \int_0^{R_{u=0}} \rho ur\, dr)_{u>0}$, is calculated by integrating $2\pi\ \rho\ ur$ from $r = 0$ to such a radial position $R_{u=0}$ where axial velocity reduces to $u = 0$ (i.e. u begins to change from $u > 0$ to $u < 0$). It is seen from Fig. 9(b) that the net increase of axial mass flux of main jet is less influenced by the shield length in the upstream region for $L_S \leq 80$ mm.

Corresponding calculated results are shown in Fig. 10 for the laminar impinging plasma jet. Figure 10(a) shows that the axial distance at which the net increase of axial mass flux of the laminar impinging plasma jet calculated by Eq. 14 begins to rise also corresponds to the shield length when $L_S \leq 80$ mm and assumes its maximum value at the section about 2 mm from the substrate surface. When the shield length increases to about 99 mm (i.e. the gap between the downstream-end section of cylindrical solid shield and the substrate decreases to 1 mm), Fig. 10(a) shows that no cold ambient air can be entrained into the jet

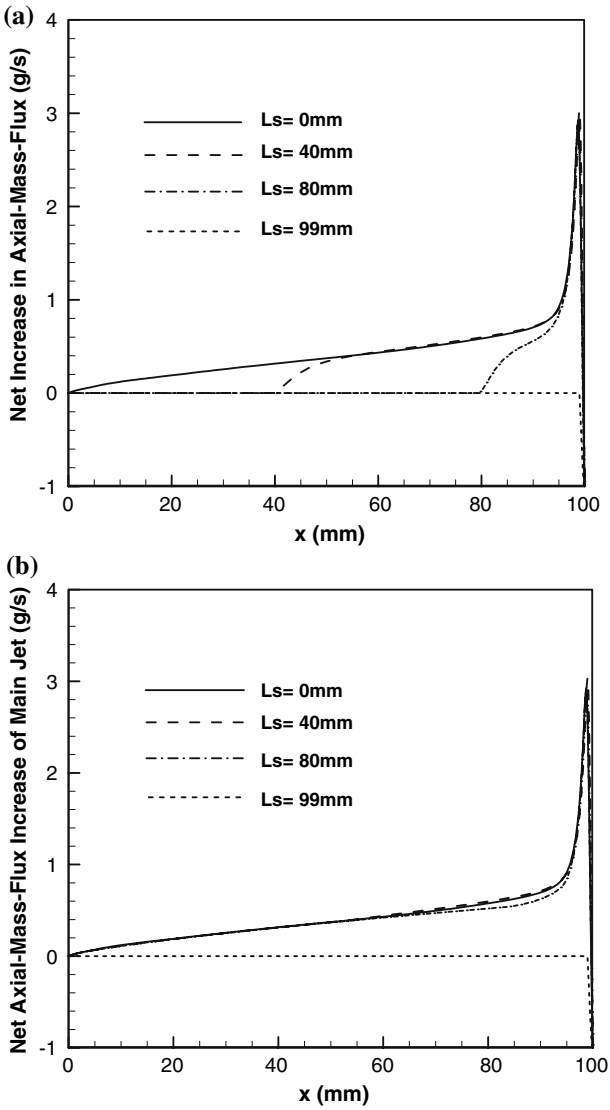

Fig. 10 Comparison of the computed variation with the axial distance of the net increase of axial mass fluxes in the laminar impinging plasma jet (**a**) and in the main jet region (**b**) for the cases with shield lengths $L_S = 0$, 40, 80 and 99 mm

region, as also seen in Fig. 7(d), and the gas entrainment of the main jet and wall jet is completely provided by the gas flowing in the large closed recirculation vortex. Figure 10(b) demonstrates that the net increase of axial mass flux of the main jet region calculated by Eq. 15 is less influenced by the shield length for $L_S \leq 90$ mm.

It is anticipated that if the ambient air can be entrained into the impinging plasma jet (e.g. when the solid shield length $L_S \leq 90$ mm), the overheating of the inner surface of the cylindrical solid shield is not a serious problem since the solid shield is protected by the entrained cold air. However, when the gap between the downstream-end section of cylindrical solid shield and the substrate surface decreases to such a value that no ambient air can be entrained (e.g. as $L_S = 95$ mm for the turbulent impinging plasma jet or $L_S = 99$ mm for the laminar impinging plasma jet), overheating of the solid shield may happen since the gas flowing in the large closed recirculation vortex will be the high-temperature argon for this case. Hence, additional computation is conducted to reveal whether the solid shield material (e.g. graphite) can endure the heating of the high-temperature recirculation gas. For this purpose the following heat transfer boundary condition

$$-\left[k\left(\frac{\partial T}{\partial r}\right)\right]_{w,sh} + \varepsilon q_r = k_\Delta \frac{(T_{wi} - T_{wo})}{\Delta} = \alpha(T_{wo} - T_a) \tag{16}$$

is employed to substitute the constant wall temperature condition (12a) at the solid shield. In Eq. 16 q_r is the local radiative heat flux incident upon the inner wall of the solid shield from the plasma jet and calculated by integrating the contribution of radiation heat transfer from the plasma in all elementary control volumes of the computational domain using the method suggested in [19]; ε is the absorptivity of the graphite wall and taken to be 0.5 [20]; k the gas thermal-conductivity; T_{wi} and T_{wo} the temperatures of the inner and outer surfaces of the solid shield, k_Δ the thermal conductivity of the shield material (20 W/(m·K) is taken in this study for graphite), Δ the thickness of the shield wall (2 mm), T_a the temperature of ambient air (300 K), whereas α is the convective heat transfer coefficient. Natural convection is assumed between the outer surface of solid shield and the ambient air, and α is calculated by the heat transfer correlation for a vertical cylinder listed in heat transfer textbooks (e.g. [21]). Calculated results show that the temperature difference between the inner and outer surfaces of the solid shield is as small as few degrees for the same axial location. The computed axial variation of inner-surface temperatures of the graphite shield wall using the convective heat transfer boundary condition (16) is shown in Fig. 11 for the case with $T_0 = 14{,}000$ K, $U_0 = 1{,}000$ m/s and $L = 100$ mm. In this figure the continuous line represents the case for the turbulent impinging plasma jet with shield length $L_S = 95$ mm, while the dashed line is for the laminar impinging plasma jet with $L_S = 99$ mm. It is seen that the highest graphite shield temperature may be as high as 3,170 K for the turbulent impinging plasma jet, while its laminar counterpart is lower than 1,300 K. The highest graphite wall temperature 3,170 K is lower than the melting temperature of graphite ($\sim$3,770 K) but appreciably higher than the temperature that graphite begins to oxidize and even to sublimate ($\sim$2,370 K) [22]. It seems that the graphite shield can endure the heating of impinging plasma jets, but using an additional measure (e.g. using a gas flow) to cool the shield wall is desired to reduce the sublimation loss of graphite shield and reduce the oxidation reaction at the outer wall of graphite shield. The computed axial variation of shield wall temperature shown in Fig. 11 for the case of laminar impinging plasma jet with $L_S = 99$ mm (dashed line) assumes a steep change at the axial location of $x = 7.5$ mm. This phenomenon is related to the appearance of a small vortex at the lateral-frontal corner in the computed flow field plotted in the upper semi-plane of Fig. 12. When

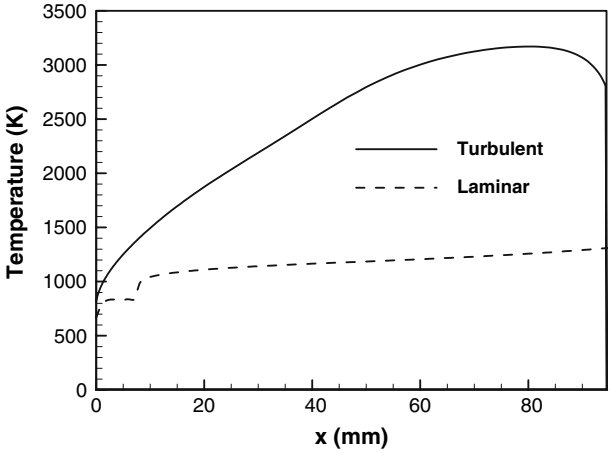

Fig. 11 Variation of computed inner-surface temperatures of graphite shield wall with the axial distance using the convective heat transfer boundary conditions. Continues line—turbulent impinging plasma jet with L_S = 95 mm; dashed line—laminar impinging plasma jet with L_S = 99 mm

the boundary condition for the energy equation is changed from the constant wall temperature condition (12a) to the convective heat transfer condition (16), the flow field of laminar impinging plasma jet also changes from that shown in the upper semi-plane of Fig. 7(d) to that shown in the upper semi-plane of Fig. 12. The computed isotherms also somewhat change from those shown in the lower semi-plane of Fig. 7(d) to those shown in the lower semi-plane of Fig. 12.

All the calculated results presented in Figs. 3–12 are for the case with the radial size of the solid shield (EF or AC in Fig. 2) being 50 mm. Additional computed results for the radial sizes 40 mm and 60 mm are presented in Fig. 13 for both the turbulent (a) and laminar (b) impinging plasma jets (with L_S = 80 mm and L = 100 mm) to compare with those for the solid shield radius 50 mm (shown in the lower semi-planes of Figs. 5(c) and 7(c)) and to show the effect of the shield radius on the flow patterns. As expected, different solid shield radii affect obviously the mass flow rate of the air entrained into the wall jet

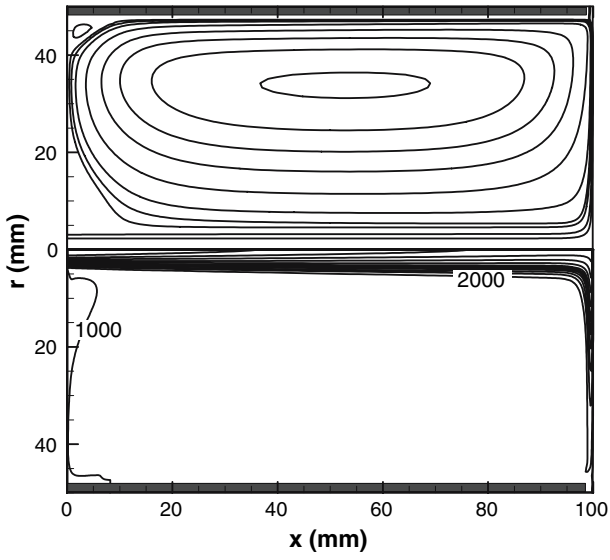

Fig. 12 Computed stream lines (upper semi-plane) and isotherms (lower semi-plane) in the laminar impinging plasma jet using the convective heat transfer boundary conditions

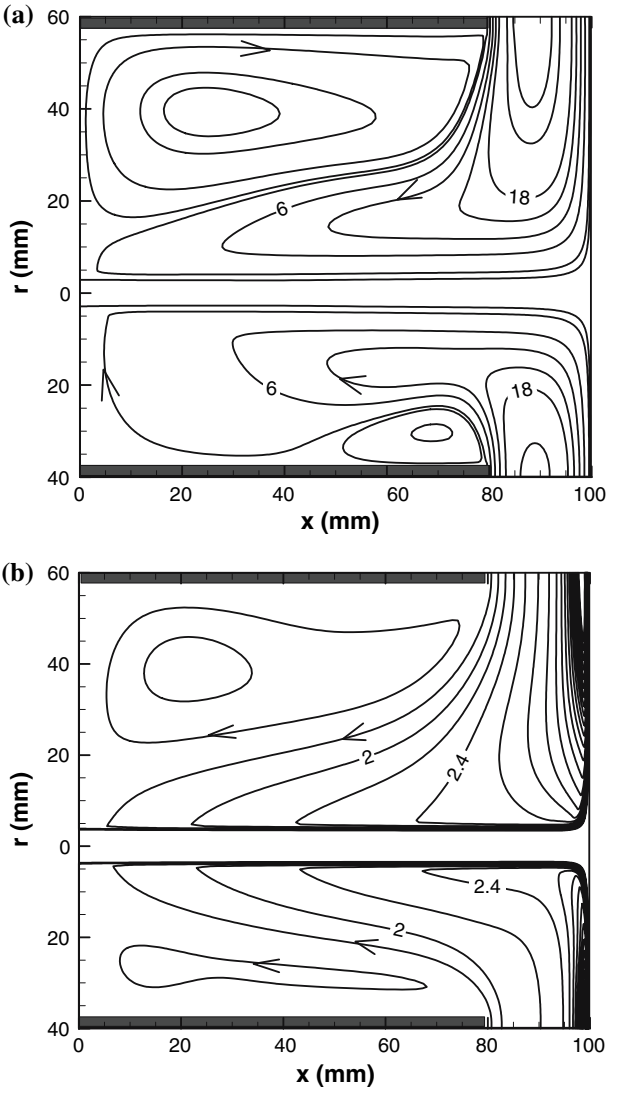

Fig. 13 Computed streamlines in the turbulent (**a**) and laminar (**b**) impinging plasma jets for the cases with shield radii of 40 mm (lower semi-planes) and 60 mm (upper semi-planes). Stream line intervals are 4×10^{-4} kg/s per radian for (**a**) and 2×10^{-5} kg/s per radian for (**b**)

region due to the change in the radial size of wall jet and affect the streamlines in the recirculation region outside the main jet, but the flow fields and thus the temperature and concentration distributions in the main jet and wall jet regions are less influenced.

Gas mixtures, such as Ar–H_2, N_2–H_2 etc. instead of pure argon, are often used as the working gas in plasma materials processing due to their higher specific enthalpy and thermal conductivity. Unfortunately, so far the species diffusion in the Ar–H_2–air or N_2–H_2–air system cannot be treated as accurately as for the Ar-air system, since Murphy's combined-diffusion-coefficient method [12, 13] cannot be simply employed for the Ar–H_2–air or N_2–H_2–air system. The modeling study involving Ar–H_2–air or N_2–H_2–air mixture must wait for the availability of an effective treatment method of the diffusion in the complex gas mixture. However, it is expected that the effects of cylindrical solid

shields on the flow patterns for the Ar–H_2–air or N_2–H_2–air system are similar to those for the Ar–air system.

Conclusions

Modeling study is conducted to show how the length of the cylindrical solid shield affects the air entrainment into the turbulent and laminar impinging argon plasma jets. It has been shown that in order to avoid the unfavorable effect of ambient air entrainment in the materials processing by use of a turbulent or laminar impinging plasma jet, the gap between the downstream-end section of the cylindrical shield and the substrate surface must be narrow enough and should be carefully chosen, since shorter solid shield cannot reduce appreciably the ambient air entrainment. Employing a cylindrical graphite shield is feasible for the turbulent impinging plasma case but attention should be paid to reduce the oxidation and sublimation loss of graphite shield wall. On the other hand, since the predicted gap size is too small for the case of laminar impinging plasma jet, an additional measure (e.g. using a shrouding gas) may be needed to avoid completely the unfavorable effect of ambient air entrainment.

Acknowledgments This work was supported by the National Natural Science Foundation of China (Grant Nos. 10772016, 50336010). The authors would like to thank Dr. A. B. Murphy who provided us the property tables for the argon-air plasmas.

References

1. Wang H-X, Chen X, Pan WX (2007) Modeling study on the entrainment of ambient air into laminar and turbulent argon plasma jets. Plasma Chem Plasma Process 27:141–162
2. Gawne DT, Zhang T, Liu B (2002) Computational analysis of the influence of a substrate, solid shield and gas shield on the flow field of a plasma jet. Surf Coat Technol 153:138–147
3. Ko TH, Chen HK (2005) Three-dimensional isothermal solid-gas flow and deposition process in a plasma spray torch with solid shield: a numerical study. Surf Coat Technol 200:2152–2164
4. Taylor TA, Overs MP, Gill BL, Tucker RC Jr (1985) Experience with MCrAl and thermal barrier coating produced via inert gas shrouded plasma deposition. J Vac Sci Technol A 3:2526–2531
5. Chen HC, Pfender E, Heberlein J (1997) Improvement of plasma spraying efficiency and coating quality. Plasma Chem Plasma Process 17:93–105
6. Thomson I, Pershin V, Mostaghimi J, Chandra S (2001) Experimental testing of a curvilinear gas shroud nozzle for improved plasma spraying. Plasma Chem Plasma Process 21:65–82
7. Henne R, Arnold J, Schiller G, Kavka T (2005) Improvement of DC thermal plasma spraying by reducing the cold gas entrainment effect. In: Proc. 2005 Int. Thermal Spray Conf., Bassel, May 2–4, 2005, pp 615–621
8. Kavka T, Henne R, Arnold J (2006) Improvement of plasma spraying conditions for SOFC applications: effect of nozzle geometry and gas shrouds. In: Proc. 2006 Int. Thermal Spray Conf., May 15–18, 2006, Seattle, Paper No. s9_8-12124
9. Kang KD, Hong SH (1999) Numerical analysis of shield gas effects on air entrainment into thermal plasma jet in ambient atmosphere of normal pressure. J Appl Phys 85:6373–6380
10. Cheng K, Chen X, Wang H-X, Pan WX (2006) Modeling study of shrouding effects on a laminar argon plasma jet impinging upon a flat substrate in air surroundings. Thin Solid Films 506–507:724–728
11. Cheng K, Chen X (2004) Prediction of the entrainment of ambient air into a turbulent argon plasma jet using a turbulence-enhanced combined-diffusion-coefficient method. Int J Heat Mass Transfer 47:5139–5148
12. Murphy AB (1993) Diffusion in equilibrium mixture of ionized gases. Phys Rev E 48:3594–3603
13. Murphy AB (1995) Transport coefficients of air, argon-air, nitrogen-air and oxygen-air plasmas. Plasma Chem Plasma Process 15:279–307

14. Cheng K, Chen X, Pan WX (2006) Comparison of laminar and turbulent thermal plasma jet characteristics – a modeling study. Plasma Chem Plasma Process 25:211–235
15. Xu D-Y, Chen X (2005) Effect of surrounding gas on the laminar jet characteristics. Int Comm Heat Mass Transfer 32:939–946
16. Williamson RL, Fincke JR, Crawford DM, Snyder SC, Swank WD, Haggard DC (2003) Entrainment in high-velocity, high-temperature plasma jets. Part II: computational results and comparison to experiment. Int J Heat Mass Transfer 46:4215–4228
17. Fincke JR, Crawford DM, Snyder SC, Swank WD, Haggard DC, Williamson RL (2003) Entrainment in high-velocity, high-temperature plasma jets. Part I: experimental results. Int J Heat Mass Transfer 46:4201–4213
18. Patankar SV (1980) Numerical heat transfer and fluid flow, Chap 6. McGraw-Hill, New York
19. Chen X (1990) Heat transfer and flow in a radio-frequency plasma torch – a new modeling approach. Int J Heat Mass Transfer 33:815–826
20. Eckert ERG, Drake RM Jr (1972) Analysis of heat and mass transfer. McGraw-Hill, New York, p 789
21. Wang BX (2002) Engineering heat and mass transfer. Science Press, Beijing, Sec. 8–3 (in Chinese)
22. Chirkin VS (1959) Thermophysical properties of materials. Physico-Mathematic Literature, Moscow, pp 333–338 (in Russian)